



RESEARCH ARTICLE

10.1029/2023JA031885

Key Points:

- Subdividing ionospheric vorticity probability density functions by the interplanetary magnetic field B_y direction allows their separation into large-scale and meso-scale components
- The large-scale vorticity relates predominantly to convection and the meso-scale vorticity to processes such as turbulence
- Models of ionospheric plasma flow need to incorporate the effects of meso-scale processes such as turbulence

Correspondence to:

G. Chisham,
gchi@bas.ac.uk

Citation:

Chisham, G., & Freeman, M. P. (2023). Separating contributions to plasma vorticity in the high-latitude ionosphere from large-scale convection and meso-scale turbulence. *Journal of Geophysical Research: Space Physics*, 128, e2023JA031885. <https://doi.org/10.1029/2023JA031885>

Received 13 JUL 2023

Accepted 18 AUG 2023

Corrected 8 SEP 2023

This article was corrected on 8 SEP 2023. See the end of the full text for details.

Author Contributions:

Conceptualization: G. Chisham, M. P. Freeman

Data curation: G. Chisham

Formal analysis: G. Chisham

Investigation: G. Chisham, M. P. Freeman

Methodology: G. Chisham

Software: G. Chisham

Visualization: G. Chisham



Writing – original draft: G. Chisham

Writing – review & editing: G. Chisham, M. P. Freeman

©2023. The Authors.

This is an open access article under the terms of the [Creative Commons Attribution License](https://creativecommons.org/licenses/by/4.0/), which permits use, distribution and reproduction in any medium, provided the original work is properly cited.

Separating Contributions to Plasma Vorticity in the High-Latitude Ionosphere From Large-Scale Convection and Meso-Scale Turbulence

G. Chisham¹  and M. P. Freeman¹ 

¹British Antarctic Survey, Cambridge, UK

Abstract Measurements of ionospheric flow vorticity can be used for studying ionospheric plasma transport processes, such as convection and turbulence, over a wide range of spatial scales. Here, we analyze probability density functions (PDFs) of ionospheric vorticity for selected regions of the northern hemisphere high-latitude ionosphere as measured by the Super Dual Auroral Radar Network over a 6-year interval (2000–2005 inclusive). Subdividing these PDFs for opposite polarities of the B_y component of the prevailing interplanetary magnetic field allows the separation into two distinct components: (a) A single-sided Weibull distribution which relates to the large-scale convection driven by magnetic reconnection; (b) A double-sided and symmetric q -exponential distribution which arises from meso-scale plasma flow related to processes such as turbulence.

Plain Language Summary This study investigates the processes that contribute to the vorticity of the flow of ionized gases (plasma) in the Earth's ionosphere (at an altitude of ~250–400 km). Vorticity is a measure of how straight or curved this flow of plasma is at a particular location. We show that the measured probability distributions of ionospheric vorticity at high-latitude locations can be explained as a combination of vorticity inherent in the large-scale ionospheric plasma flow pattern driven by variations in the solar wind (plasma and magnetic field ejected by the Sun), and vorticity resulting from meso-scale fluid processes such as turbulence. Being able to model ionospheric vorticity in this way helps to improve models of the ionospheric flow process, which are often key components of larger operational space weather models.

1. Introduction

The large-scale behavior of ionospheric plasma flow at high latitudes is dominated by the convection flow driven by magnetic reconnection at the Earth's magnetopause and within its magnetotail (Chisham, Freeman, et al., 2008; Hubert et al., 2006; Milan et al., 2003). This large-scale behavior is well understood (Cowley & Lockwood, 1992; Lockwood et al., 1990; Milan et al., 2012; Siscoe & Huang, 1985), and provides the basis for the understanding and modeling of magnetosphere-ionosphere (M-I) coupling processes. However, at meso- and small-scales, other processes such as turbulence are responsible for structure in the ionospheric plasma flow over a range of scales (~1–1,000 km) (Abel et al., 2006, 2009, 2007; Chaston et al., 2008; Kintner & Seyler, 1985; Tsunoda, 1988). Turbulence is characterized by intermittency, where the occurrence of extreme values is more likely than expected from a normal distribution (e.g., Frisch, 2010, and references therein). Understanding and quantifying this intermittency is important for developing probabilistic forecasting models of space weather.

One measure often used to quantify turbulence in a fluid is vorticity; measurements of vorticity help to characterize the structure of the flow of a fluid. The vorticity of plasma flow in the ionosphere has been estimated for many years from measurements of ionospheric plasma velocity made by high-frequency (HF) coherent-scatter radars in the Super Dual Auroral Radar Network (SuperDARN) (Sofko et al., 1995). In the first statistical study of SuperDARN ionospheric vorticity, Chisham et al. (2009) showed that the large-scale spatial variation of average vorticity in the ionosphere varies in a very similar way to that of the average magnetic field-aligned current (FAC) (Anderson et al., 2008). Consequently, we use the same “Region” terminology for ionospheric vorticity as is used for FACs (Iijima & Potemra, 1976).

Measurements of vorticity using SuperDARN are limited to the large (~1,000 km) and meso-scales (~100 km) due to the typical SuperDARN range gate size (~45 km). At present it is not possible to easily measure ionospheric vorticity at scales smaller than this. However, the presence of ionospheric turbulence and intermittency at

smaller scales (<1–10 km) has been measured in rocket measurements of ionospheric electron density and electric field (Di Mare et al., 2021; Spicher et al., 2022, 2015). Indeed, decameter-scale electron density irregularity structures, related to this small-scale turbulence, form the ionospheric scattering targets for the SuperDARN radar HF signals. SuperDARN measurements of Doppler spectral width and velocity error can often provide an indirect measure of the level of this sub-grid scale structure and turbulence (Spicher et al., 2022; Vallières et al., 2004).

Measuring and modeling the probability density functions (PDFs) of large and meso-scale ionospheric vorticity measured by SuperDARN have helped provide a statistical understanding of the ionospheric plasma flow. PDFs of ionospheric vorticity are typically highly leptokurtic (higher kurtosis than a Gaussian) throughout the polar ionosphere (Chisham & Freeman, 2010, 2021), showing that the plasma flow is characterized by intermittency. Measured PDFs of vorticity have shown that large-scale averaged pictures of vorticity and its spatial variation are gross simplifications of the true picture. The measured vorticity at any location can be vastly different from, and often significantly larger than, the average (Chisham & Freeman, 2021).

Chisham and Freeman (2010) were first to model the observed PDFs of vorticity, treating the positive and negative vorticities independently. (Due to the observed asymmetry of the PDFs at many locations, it has been usual to model the positive and negative distributions independently). They compared the goodness of fit of three potential leptokurtic model distributions (q -exponential, Weibull, exponential) to the observed PDFs using maximum likelihood estimation (MLE). In most regions, the q -exponential proved the best fit of the three model distributions, except in the dayside Region 1 (R1), where the Weibull was occasionally a better fit.

Chisham and Freeman (2021) later took the decision to model the observed PDFs at all locations with q -exponential distributions. The basis of this decision was that the Weibull distribution tends toward either zero or infinity as the observed variable tends toward zero. Chisham and Freeman (2021) showed that the PDFs of vorticity were clearly continuous through both zero and the mode of the distribution (which is typically shifted slightly from zero). They presented, for the first time, the spatial variation of the model q -exponential parameters across the northern hemisphere polar ionosphere, and showed how these model distributions can be used to estimate the likelihood of extreme vorticity at any location. They also showed that the average values of vorticity observed in R1 were not a result of a shift in the mean of a symmetric PDF, but were due to asymmetries in the PDFs around zero vorticity. These asymmetries (and consequently the average vorticity values) were opposite in the regions either side of noon and midnight, explaining the spatial variations of average vorticity presented in Chisham et al. (2009).

Following recommendations made in Chisham and Freeman (2021), Coxon et al. (2022) applied the same analysis methods to PDFs of FACs measured by the Active Magnetosphere and Planetary Electrodynamics Response Experiment (AMPERE) (Anderson et al., 2014; Waters et al., 2001). FACs are intimately related to vorticity, being proportional in the limit of uniform ionospheric conductance, and the results presented by Coxon et al. (2022) showed that PDFs of FAC are similarly leptokurtic, with a similar spatial variation of q -exponential fit parameters across the northern hemisphere polar ionosphere. They used these results to identify regions of the ionosphere where there is a high likelihood of extreme FACs.

Following on from these phenomenological studies, it is important to be able to understand the observed asymmetries in the vorticity PDFs, and what processes are responsible for these variations. For example, Chisham and Freeman (2021) discussed how mixing vorticity measurements with different drivers and sources might affect the observed PDFs. These mixture distributions were mainly discussed in the context of the expanding-contracting polar cap paradigm (Cowley & Lockwood, 1992; Milan, 2013), relating to the effects of combining observations from different topological regions (e.g., auroral zone and polar cap) in PDFs measured at a fixed physical coordinate (Chisham, 2017). However, they also discussed the mixture distributions that result from combining vorticity data measured during times of oppositely directed interplanetary magnetic field (IMF) B_y . Changes in IMF B_y introduce asymmetries in the spatial structure of ionospheric convection (Cowley & Lockwood, 1992), and hence in the magnetic local time (MLT) extents of the large-scale dayside FAC and vorticity regions (Chisham et al., 2009).

We postulate here that the observed ionospheric vorticity PDFs at many locations may be a consequence of a mixture distribution of vorticity from two different sources: (1) vorticity due to the large-scale plasma convection flow (which we assume is highly variable with IMF B_y); and (2) vorticity resulting from meso-scale processes such as turbulence (which we assume varies little with IMF B_y). Hence, here we separate observations for opposite IMF B_y states to investigate whether the observed PDFs can be described by such mixture distributions.

The paper is structured as follows: In Section 2 we describe the ionospheric vorticity data set. Section 3 presents the results of the analysis. In Section 4 we propose a model that allows us to deconvolve the vorticity PDFs into components resulting from the large-scale and meso-scale processes. Section 5 presents a discussion of the results and their potential interpretation. Section 6 summarizes and concludes the paper.

2. Methodology

In this study we use ionospheric vorticity measurements made by SuperDARN. SuperDARN is a network of HF radars designed to measure large- and meso-scale plasma flow in the polar and mid-latitude ionosphere in both hemispheres (Chisham et al., 2007; Greenwald et al., 1995; Nishitani et al., 2019). The method for estimating ionospheric vorticity from line-of-sight SuperDARN velocity measurements is outlined in detail in Chisham et al. (2009) and Chisham and Freeman (2021), and is similar to that proposed by Sofko et al. (1995). It requires measuring the ionospheric plasma velocity around closed loops defined by the overlapping beams in the SuperDARN radar geometry. These closed loops enclose measurement cell areas ranging in size from $\sim 5,000$ km², for the smallest cells nearest the radars (lower latitudes), to $\sim 50,000$ km², for the largest cells furthest from the radars (higher latitudes). The typical cell size is $\sim 10,000$ – $20,000$ km². In these analyses, the vorticity measurement location for a cell is taken as the geometric center of the area defined by the closed loop.

Here, we use the same 6-year data set of ionospheric vorticity measurements (2000–2005 inclusive) as in the previous studies discussed above (Chisham, 2023). This data set contains ~ 11 million vorticity measurements covering a wide range of latitudes and local time in the northern hemisphere polar region. These measurements are subdivided by their latitude and MLT to create PDFs of vorticity that represent particular spatial regions, as described in the following section. In this data set, a positive field-aligned vorticity (clockwise rotation when looking in the direction of the magnetic field into the northern hemisphere ionosphere) is related to an upward FAC, whereas a negative field-aligned vorticity (anticlockwise rotation when looking in the direction of the magnetic field into the northern hemisphere ionosphere) is related to a downward FAC.

The vorticity data have also been organized by the prevailing IMF direction. The vorticity data were initially subdivided into eight subgroups defined by the prevailing IMF state, as in Chisham et al. (2009). Each subgroup relates to a 45° IMF clock angle bin in the Geocentric Solar Magnetospheric Y – Z plane. To determine the IMF clock angle at any one time we use 1-min IMF data from OMNIWeb, that is already lagged from the spacecraft to the Earth's bow shock. We also restrict our analysis to relatively stable IMF intervals, where 70% of the IMF data within the prevailing 30-min interval was contained within a single clock angle bin, consistent with the analysis of Chisham et al. (2009). For most of this study, we only use data in the two 45° bins centered around the B_y axis, representing IMF B_y positive and IMF B_y negative. We compile vorticity PDFs for both these IMF states for each spatial bin.

3. Results

As discussed in Section 1, changes in the IMF introduce asymmetries in the spatial structure of the large-scale ionospheric convection. In Figure 1 we present (as solid black lines) climatological patterns of ionospheric convection from the statistical model of Thomas and Shepherd (2018), which was derived from SuperDARN line-of-sight velocity data. The figure presents the model equipotentials of northern hemisphere ionospheric convection at 4-kV intervals (black contours) for the eight different 45° IMF clock angle bins, for neutral dipole tilt and moderate solar wind driving conditions. (The central direction of each clock angle bin is marked by the dial in the center of Figure 1). These equipotentials equate to the average streamlines of the ionospheric plasma flow during these conditions.

Coincident with the large-scale ionospheric convection variations in Figure 1, we present the spatial variation of the average ionospheric vorticity across the northern hemisphere polar region, as first derived by Chisham et al. (2009). These average vorticity values are determined from PDFs covering the 6 years of vorticity measurements grouped in spatial bins of size 1° of Altitude-Adjusted Corrected GeoMagnetic (AACGM) latitude by 1 hr of MLT. The darker orange regions represent areas of higher negative (anticlockwise) average vorticity, equivalent to regions of downward FAC. The darker blue regions represent areas of higher positive (clockwise) average vorticity, equivalent to regions of upward FAC.

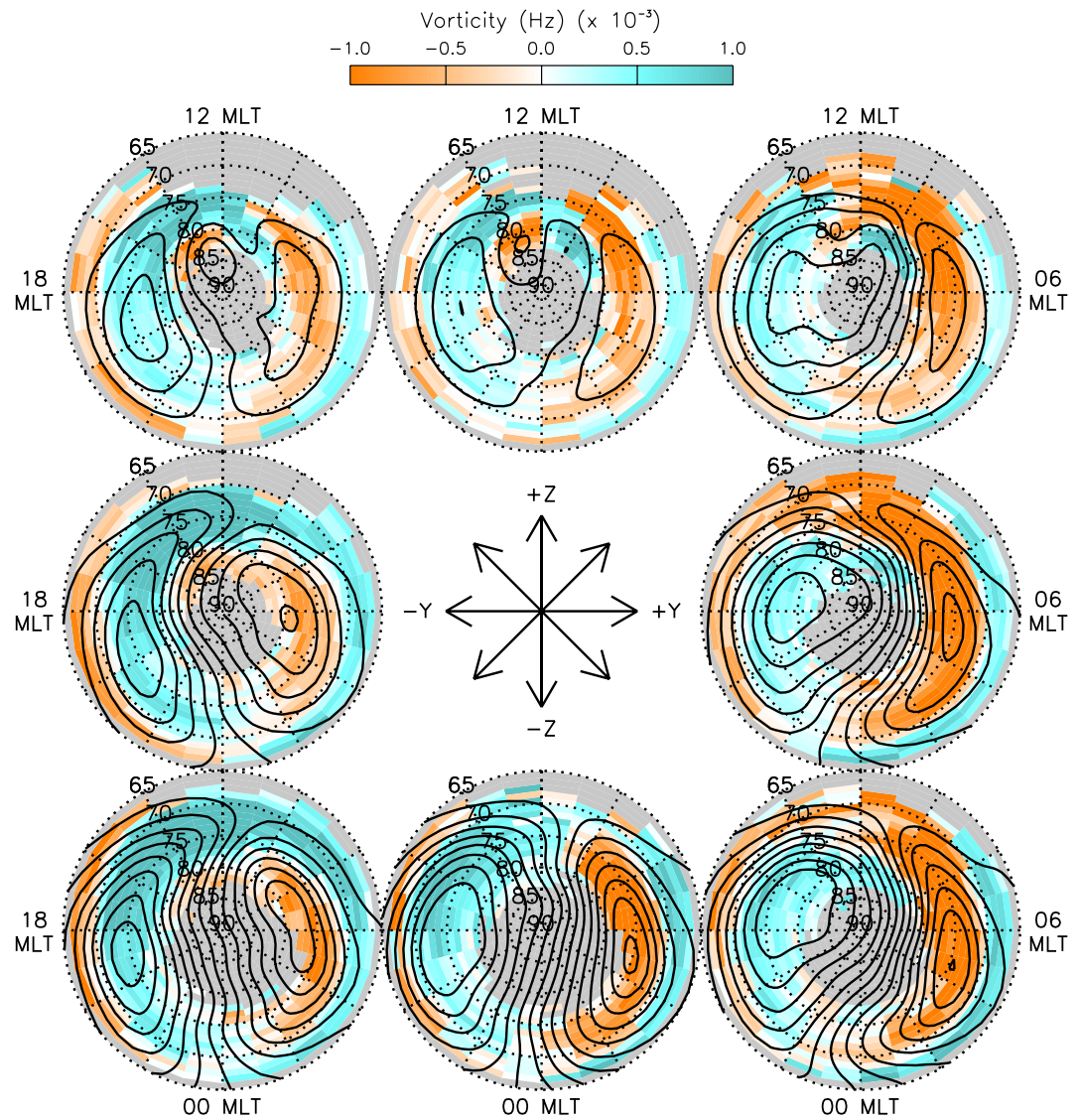


Figure 1. Patterns of average vorticity for 6 years of SuperDARN vorticity measurements in Altitude-Adjusted Corrected GeoMagnetic (AACGM) and magnetic local time (MLT) coordinates, separated by the interplanetary magnetic field (IMF) clock angle direction. The central direction of each 45° clock angle bin for each map is shown by the dial in the center. The gray regions represent areas where there are not enough vorticity measurements to determine a reliable and representative average. The solid black lines represent climatological patterns of ionospheric convection from the model of Thomas and Shepherd (2018) for neutral dipole tilt and moderate solar wind driving conditions. The black contours represent equipotentials of ionospheric convection at 4-kV intervals.

As discussed in Chisham et al. (2009), the local time extents of the average vorticity regions change with the direction of the IMF. By comparing the convection flow streamlines and the average vorticity in Figure 1, it is clear that there is a relationship between regions of large rotation, or shears, in the climatological convection flow and larger values of average vorticity in the same sense as the shear flow. This is as would be expected even though these parameters have been determined using different methodologies and data intervals. However, we know from the work of Chisham and Freeman (2021) that these average values are a result of asymmetries in the vorticity PDFs. Hence, it seems likely that these asymmetries are associated with the regions of high vorticity in the climatological convection flow.

These initial observations direct our choice of data selection for further analysis. The most extreme differences in statistical convection and average vorticity between the different IMF clock angle directions occurs in the dayside R1 for opposite IMF B_y conditions. Here, the dayside R1 is dominated by a positive average vorticity relating to

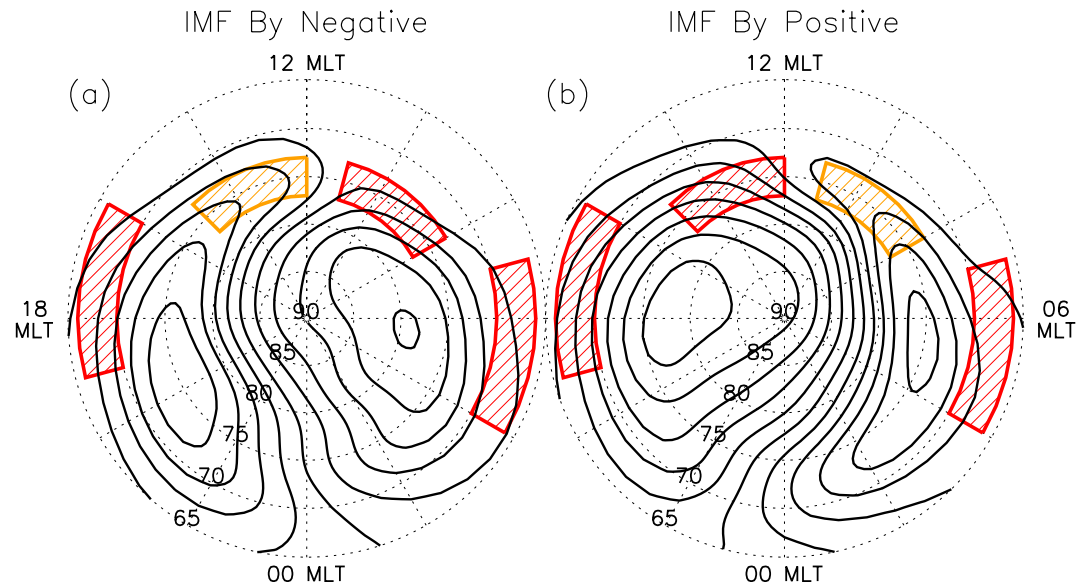


Figure 2. Climatological patterns of large-scale ionospheric convection from the model of Thomas and Shepherd (2018) for neutral dipole tilt and moderate solar wind driving conditions. The black contours represent equipotentials of ionospheric convection at 4-kV intervals. The red and orange hatched regions either side of noon represent the regions for which we show the associated probability density functions (PDFs) in Figure 3. The red hatched regions that straddle dawn and dusk represent the regions for which we show the associated PDFs in Figure 4.

shear flow in the dusk convection cell for negative IMF B_y , and a negative average vorticity relating to shear flow in the dawn convection cell for positive IMF B_y . Hence, we concentrate on the differences between the vorticity observations for these two IMF clock angle directions in the rest of the paper.

In Figure 2, we show again the climatological patterns of the large-scale ionospheric convection for these two IMF clock angle directions: (a) IMF B_y negative conditions and (b) IMF B_y positive conditions. For our analysis, we choose to compile PDFs covering the 6 years of vorticity measurements in four selected spatial bins of size 4° of AACGM latitude by 3 hr of MLT, two in the dayside R1 and two in R2 around dawn and dusk. The hatched regions delineate the selected spatial bins for our PDF analysis. The orange-hatched regions in Figure 2 are characterized by large-scale convection flow reversals, and hence large-scale vorticity due to the convection flow. In contrast, the red-hatched regions are characterized by straighter flow streamlines and lower large-scale vorticity.

Next, we present the observed PDFs for these four regions of interest. We start by considering the dayside R1 variations in the dawn convection cell. The orange-hatched region for IMF B_y positive in Figure 2b (73° – 77° AACGM latitude and 0800 to 1100 MLT), contains a region of significant large-scale convection flow reversal associated with a negative vorticity. The same (but red-hatched) region for IMF B_y negative in Figure 2a contains straighter flow streamlines and hence, a lower magnitude large-scale vorticity in the convection flow. Figure 3a presents the observed PDFs for the R1 dawn cell hatched region for both IMF B_y positive (red symbols and solid lines) and IMF B_y negative (black symbols and lines). These PDFs are determined from 51,042 and 30,240 vorticity measurements for IMF B_y positive and IMF B_y negative, respectively. The symbols represent regularly binned PDF values. During times of IMF B_y negative (black), for which this region is not characterized by reversals in the large-scale convection flow, the PDF variations for both positive and negative vorticity are approximately symmetric, with both being slightly more leptokurtic than an exponential (a straight line on this log-linear plot). In contrast, during times of IMF B_y positive (red), for which this region is characterized by a significant negative vorticity in the large-scale convection flow, the PDF variations for positive and negative vorticity are distinctly different. Whereas the positive vorticity variation is very similar to those seen for IMF B_y negative, the negative vorticity variation is characterized by a bulge, with the observed PDF being significantly less leptokurtic than an exponential. This asymmetry results in the large negative average vorticity in this region as seen in Figure 1.

We move next to consider the dayside R1 variations in the dusk convection cell. The orange-hatched region for IMF B_y negative in Figure 2a (73° – 77° AACGM latitude and 1200 to 1500 MLT), contains a region of

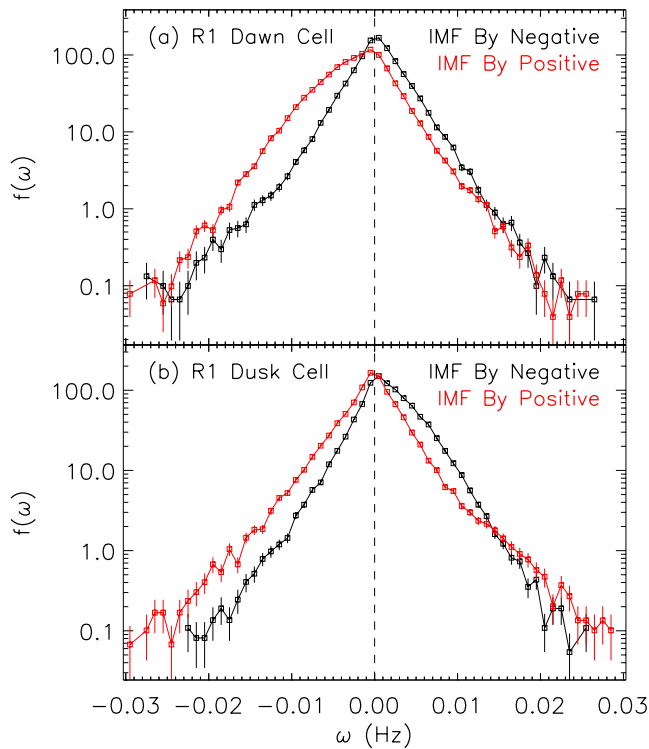


Figure 3. (a) Probability density functions (PDFs) of vorticity for a portion of the Region 1 dawn cell [73°–77° Altitude-Adjusted Corrected GeoMagnetic (AACGM) latitude and 0800 to 1100 magnetic local time (MLT)]. (b) PDFs of vorticity for a portion of the Region 1 dusk cell (73°–77° AACGM latitude and 1200 to 1500 MLT). In both panels the black distributions represent those for interplanetary magnetic field (IMF) B_y negative, whereas the red distributions represent those for IMF B_y positive. The symbols and error bars represent the binned PDF values.

significant large-scale convection flow reversal associated with a positive vorticity. The same (but red-hatched) region for IMF B_y positive in Figure 2b contains straighter flow streamlines and hence, lower large-scale vorticity in the convection flow. Similar to the R1 dawn cell PDFs in Figure 3a, Figure 3b presents the PDFs for the R1 dusk cell hatched region for both IMF B_y positive (red symbols and solid lines) and IMF B_y negative (black symbols and lines). These PDFs are determined from 29,678 and 36,860 vorticity measurements for IMF B_y positive and IMF B_y negative, respectively. During times of IMF B_y positive (red), for which this region is not characterized by reversals in the large-scale convection flow, the PDF variations for both positive and negative vorticity are similar, with both being more leptokurtic than an exponential. In contrast, during times of IMF B_y negative (black), for which this region is characterized by a significant positive vorticity in the large-scale convection flow, the PDF variations for positive and negative vorticity are distinctly different. Whereas the negative vorticity variation is similar to those seen for IMF B_y positive, the positive vorticity variation is characterized by a bulge (similar to that in Figure 3a for IMF B_y positive, but of the opposite vorticity sign), with the observed PDF being significantly less leptokurtic than an exponential. This asymmetry results in the large positive average vorticity in this region as seen in Figure 1.

Hence, these results suggest that the existence of reversals in the large-scale dayside convection flow have a significant impact on the asymmetry in the observed R1 PDFs, reducing the kurtosis on one side of the distribution, and increasing the mean value on that side of the distribution.

Finally, we consider the Region 2 (R2) variations in both the dawn convection cell (66°–70° AACGM latitude and 0400 to 0700 MLT) and the dusk convection cell (66°–70° AACGM latitude and 1600 to 1900 MLT), as shown by the red-hatched regions at lower latitudes around dawn and dusk in Figures 2a and 2b. Both these regions, for both IMF B_y directions, are characterized by relatively straight flow streamlines in Figures 1 and 2, with no large-scale vorticity in the convection flow. Figure 4 presents the PDFs for these two hatched regions, in the same format as Figure 3. Figure 4a presents

the PDFs for the R2 dawn cell, and Figure 4b presents the PDFs for the R2 dusk cell. The PDFs for the dawn cell are determined from 29,002 and 32,056 vorticity measurements for IMF B_y positive and IMF B_y negative, respectively. The PDFs for the dusk cell are determined from 15,278 and 21,046 vorticity measurements for IMF B_y positive and IMF B_y negative, respectively. The PDFs observed in both locations are roughly symmetric, and more leptokurtic than those measured for the R1 vorticity in Figure 3. This is consistent with the results presented in Chisham and Freeman (2021). The PDFs in both locations, and for both IMF B_y directions, are very similar, suggesting similar vorticity characteristics in these two regions, and for the different IMF directions. The only difference between the dawn and dusk cell R2 PDFs appears to be a small shift in the mode of the PDF to a positive value in the dawn cell, and to a negative value in the dusk cell. This matches the differences in the average vorticity values seen in these regions for all IMF clock angle directions, as shown in Figure 1. These results suggest that variations in the IMF have no effect on vorticity in R2.

4. Model

We propose a simple model to explain the observed asymmetry in the dayside R1 PDF variations. We propose that the observed vorticity PDFs are a mixture of vorticity related to variations in the large-scale convection flow (henceforth termed the “LS” component) and to meso-scale variations from processes such as turbulence (henceforth termed the “MS” component).

First, we propose that the MS vorticity PDF is leptokurtic (as expected due to intermittency), and broadly symmetric around zero (i.e., there is no preferred sense to vorticity at this scale). We propose that this PDF is well modeled by a q -exponential distribution, as suggested by the analyses of Chisham and Freeman (2010)

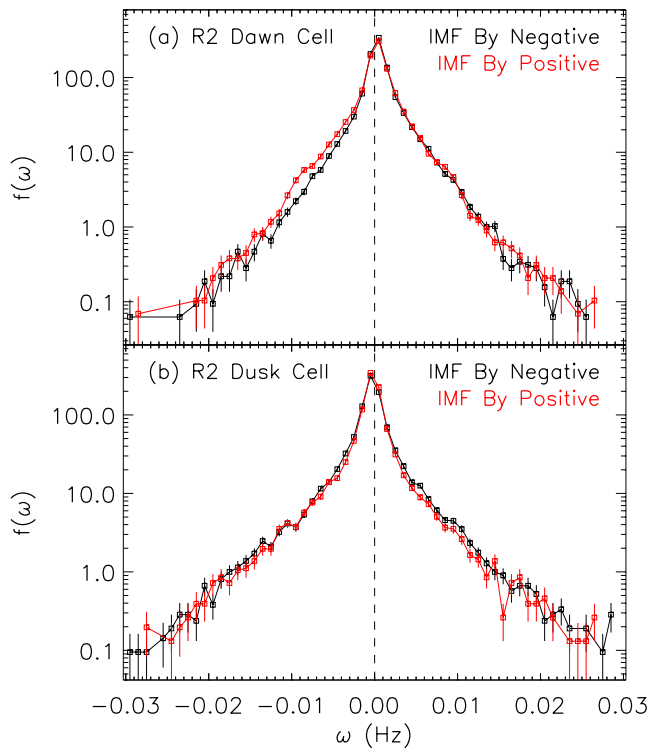


Figure 4. (a) Probability density functions (PDFs) of vorticity for a portion of the Region 2 dawn cell [66°–70° Altitude-Adjusted Corrected GeoMagnetic (AACGM) latitude and 0400 to 0700 magnetic local time (MLT)]. (b) PDFs of vorticity for a portion of the Region 2 dusk cell (66°–70° AACGM latitude and 1600 to 1900 MLT). In both panels the black distributions represent those for interplanetary magnetic field (IMF) B_y negative, whereas the red distributions represent those for IMF B_y positive. The symbols and error bars represent the binned PDF values.

and Chisham and Freeman (2021). We follow the methodology presented in Chisham and Freeman (2021), where vorticity PDFs are modeled by q -exponential distributions of the form

$$f_{q,\kappa}(\omega) = \frac{1}{\kappa} \left(1 - \frac{(1-q)\omega}{\kappa} \right)^{q/(1-q)} \quad (1)$$

using MLE. Here, q and κ are the parameters that define the distribution. q describes the distribution shape and is associated with the level of kurtosis in the distribution, and κ describes the distribution scale and is associated with the mean of the single-sided distribution (and hence, the variance of the double-sided distribution). The q -exponential distributions are exponential when q equals 1 and become increasingly heavy-tailed as q increases greater than 1.

Second, we propose that on the spatial scales that we are measuring the individual PDFs, that the LS vorticity PDF is single-sided (i.e., there is only a single sense to the large-scale vorticity direction in each measurement cell). Following the theoretical arguments presented in Chisham and Freeman (2010), we propose that the PDFs of the R1 LS flow vorticity are better modeled by a single-sided Weibull function of the form

$$f(\omega) = \frac{c}{\chi} \left(\frac{\omega}{\chi} \right)^{c-1} \exp \left[- \left(\frac{\omega}{\chi} \right)^c \right] \quad (2)$$

where c and χ represent the shape and scale parameters of the model fit, and where the function becomes an exponential when c equals 1.

Figure 5a shows again the vorticity PDF for the R1 dawn cell during intervals of IMF B_y positive, as shown originally in Figure 3a. Following our assumptions, the highly leptokurtic positive vorticity PDF is taken as comprising wholly of MS vorticity. These data have been fit with a q -exponential function with fit parameters $q = 1.05$ and $\kappa = 0.0025$, which provides a good fit to the data. The negative vorticity PDF is taken as comprising a mixture of the MS and LS vorticity components, so these data have not been fit by a single function.

Figure 5b presents the deconstruction of the observed vorticity PDF into the MS component (black) and the LS component (red), by following the above assumptions. The PDF variation (and the q -exponential model fit) for positive vorticity is the same as in Figure 5a, as the large-scale convection flow contributes only to the negative vorticity PDF in this location. Our assumption that the MS vorticity PDF is symmetric around zero means that this PDF (black symbols) is identical for both positive and negative vorticity (as is the q -exponential model fit). The LS PDF is determined by subtracting the binned MS PDF values from the combined PDF values presented in Figure 5a, and is presented as red symbols in Figure 5b. The red line shows a Weibull fit to the PDF with fit parameters $c = 1.6$ and $\chi = 0.0065$. The Weibull fit to the PDF is good, justifying our decision to fit this theoretical distribution to the LS PDF.

Figure 5c shows how the balance between the two components varies with the magnitude of the vorticity, by showing the percentage contribution of each component to the measured PDF in Figure 5a. This is calculated for both the binned PDF values (square symbols), and the model fits (solid lines). This shows how the negative vorticity due to the large-scale variations in convection dominates over that due to meso-scale processes such as turbulence from ~ 2 mHz to ~ 23 mHz with the meso-scale processes dominating at the smallest and largest magnitude vorticities. However, results at vorticity magnitudes greater than ~ 0.02 Hz should be viewed with skepticism due to the increasingly low count levels.

Mirroring the R1 dawn cell analysis in Figure 5, Figure 6a shows the vorticity PDF for the R1 dusk cell during intervals of IMF B_y negative, as shown originally in Figure 3b. Again following our assumptions, the highly

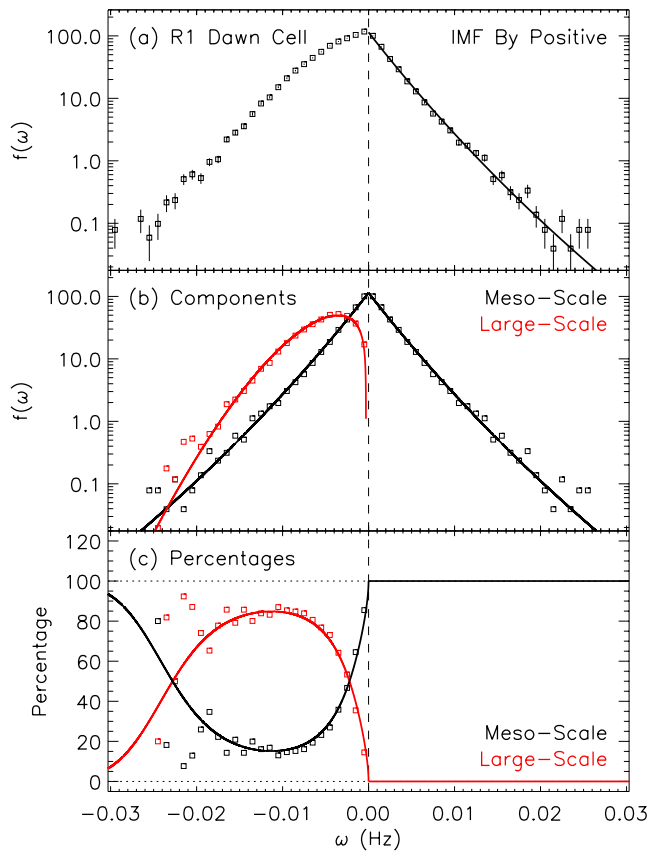


Figure 5. (a) Probability density function (PDF) of vorticity for a portion of the Region 1 dawn cell [73°–77° Altitude-Adjusted Corrected GeoMagnetic (AACGM) latitude and 0800 to 1100 magnetic local time (MLT)] for interplanetary magnetic field (IMF) B_y positive. The symbols and error bars represent the binned PDF values, whereas the solid line shows the maximum likelihood estimation (MLE) q -exponential fit to the data. (b) PDFs of vorticity from the same region deconstructed into the meso-scale (MS) component (black) and the large-scale (LS) component (red). The symbols represent the binned PDF values. The black solid lines show the q -exponential fits to the MS PDFs, whereas the red solid line shows a Weibull fit to the LS PDF. (c) The percentage contribution of each component in panel (b) to the measured PDF in panel (a). The symbols represent the percentages determined using the binned PDF values, whereas the solid lines represent the percentages determined using the model fits.

leptokurtic negative vorticity PDF is taken as comprising wholly of the MS vorticity PDF. These data have been fit with a q -exponential function with fit parameters $q = 1.13$ and $\kappa = 0.0020$, which again provides a good fit to the data. Again, the positive vorticity PDF is taken as comprising a mixture of the MS vorticity PDF and the LS vorticity PDF.

Following the same methodology as the previous example in Figure 5, Figure 6b presents the deconstruction of the observed vorticity PDF into the MS component (black) and the LS component (red). Here, the LS PDF (red symbols) occurs solely in the positive vorticity direction, matching the large-scale vorticity observed in the dusk region. The red line shows a Weibull fit to the PDF with fit parameters $c = 1.4$ and $\chi = 0.0045$. Again, the Weibull fit to the PDF is good, further justifying our decision to fit this theoretical distribution to the LS PDF.

Figure 6c follows the presentation of Figure 5c to show the balance between the two components. In this case the LS component dominates over the MS component for a smaller range of vorticity magnitude, from ~ 2 mHz to ~ 18 mHz. The MS component dominates at the smallest and largest vorticities. Again, the results at larger vorticity magnitudes should be treated with skepticism.

5. Discussion

5.1. Measurement Uncertainties

Before attempting a scientific interpretation of the observed vorticity PDFs, we must assess the contribution of measurement errors and uncertainties. As with all measured or derived quantities, there is a level of uncertainty in the individual vorticity estimates. As a consequence, the measured PDFs are a convolution of the “real” PDFs which represent the true vorticity distribution, with another distribution that represents these measurement and algorithmic errors and uncertainties.

As discussed in Section 1, sub-grid scale fluctuations and their variability over the SuperDARN measurement timescale is a major source of uncertainty in SuperDARN velocity measurements, and consequently in vorticity estimations. Chisham and Freeman (2021) also discussed other potential sources of uncertainty in the vorticity estimations. They include factors associated with the measurement technique such as missing or poor velocity estimates around the closed loops used to determine the vorticity (Chisham et al., 2009), and inaccuracies in the geolocation mapping of the SuperDARN velocity measurements (Chisham, Yeoman, & Sofko, 2008). It is also likely that the size of

these uncertainties will vary with the measurement scale, that is, with the size of the closed loops formed by the overlapping radar beams. The loop size increases with distance from the radars owing to the divergence of the radar beams (Chisham et al., 2009).

As yet, no attempt has been made to estimate or simulate the PDFs of vorticity that would arise purely from measurement errors, uncertainties, and sub-grid scale structure. Here, we attempt to simulate these distributions based on the distributions of observed SuperDARN velocity errors in typical R1 and R2 locations. For this simulation we make use of data from the Prince George (PGR) SuperDARN radar only, which is one of the radars used to develop the vorticity data set (Chisham & Freeman, 2021; Chisham et al., 2009). We analyze data from a single PGR beam (beam 12) using the most recent SuperDARN analysis algorithm (FitACF v3.0) and produce PDFs of the velocity error (a standard output of the FitACF method) for all range gates along this beam, using all data from 2000 to 2005 inclusive (the same interval used to determine the vorticity data set). Only data with a signal-to-noise ratio greater than 3 dB, and classified as ionospheric scatter by the standard SuperDARN algorithm, were used in the compilation of the velocity error distributions. To simulate the vorticity uncertainty PDFs

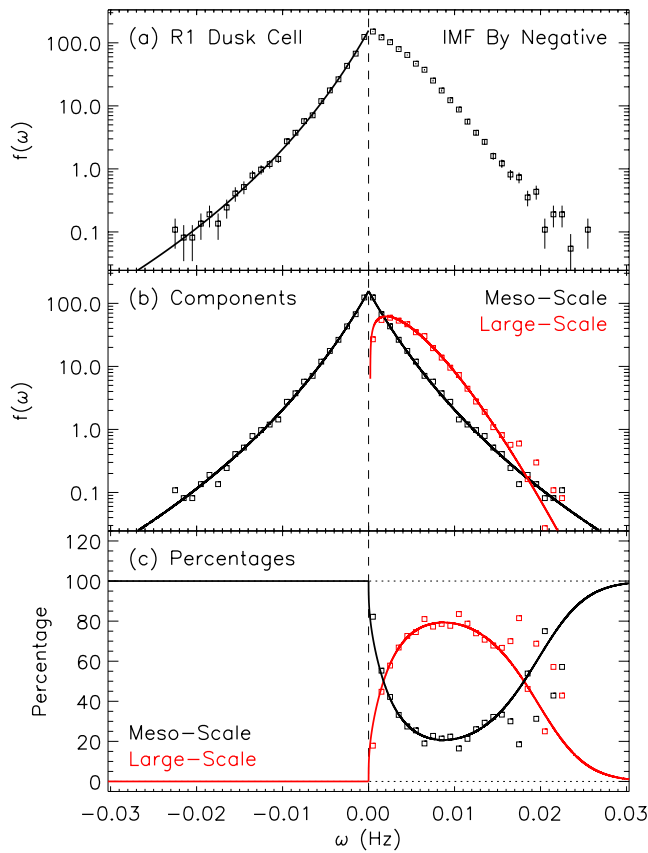


Figure 6. (a) Probability density functions (PDFs) of vorticity for a portion of the Region 1 dusk cell [73°–77° Altitude-Adjusted Corrected GeoMagnetic (AACGM) latitude and 1200 to 1500 magnetic local time (MLT)] for interplanetary magnetic field (IMF) B_y negative. The symbols and error bars represent the binned PDF values, whereas the solid line shows the maximum likelihood estimation (MLE) q -exponential fit to the data. (b) PDFs of vorticity from the same region deconstructed into the meso-scale (MS) component (black) and the large-scale (LS) component (red). The symbols represent the binned PDF values. The black solid lines show the q -exponential fits to the MS PDFs, whereas the red solid line shows a Weibull fit to the LS PDF. (c) The percentage contribution of each component in panel (b) to the measured PDF in panel (a). The symbols represent the percentages determined using the binned PDF values, whereas the solid lines represent the percentages determined using the model fits.

we simulate the “flow” around a closed measurement loop that is purely due to velocity errors. That is the situation that occurs with zero, or constant (in speed and direction), background flow. In this instance, any vorticity that is measured is purely a result of the velocity errors.

First, we simulate a PDF of vorticity uncertainties that is typical of R1. We simulate a closed measurement loop that is of a typical size for this region, forming a square with a length of three SuperDARN range gates (135 km) on each side. This produces a measurement cell of size $\sim 18,000$ km², which is typical of this region (Chisham et al., 2009). For each of the 12 simulated “velocity” measurements around the closed loop, we randomly select velocity error values from the measured distribution for beam 12, range gate 45 (which is centered in the R1 location), and multiply this value by a randomly selected value from a normal distribution of mean 0 and standard deviation 1. This simulates the random selection of a “velocity” value from an error distribution with a standard deviation given by the randomly selected velocity error value. We then combine these “velocity” measurements to produce a “vorticity” value using the methods outlined in Chisham et al. (2009). To produce the simulated PDF of vorticity uncertainties, we simulate 10^6 different “vorticity” values. Figure 7a presents the resulting vorticity PDF (black symbols and lines). The red lines show, for comparison, the PDF for the R1 dusk cell for IMF B_y positive conditions, as shown in Figure 3b. It is clear from this that the uncertainty PDF has a much lower variance than the observed vorticity PDF in this region, suggesting that it only has a small impact on the character of that distribution.

Second, we repeat this simulation to produce a PDF of vorticity uncertainties that is typical of R2. In this case, we simulate a closed measurement loop that forms a square with a length of two range gates (90 km) on each side. This produces a measurement cell of size $\sim 8,000$ km², which is typical of this region (Chisham et al., 2009). For each of the eight simulated velocity measurements around the closed loop, we randomly select velocity error values from the measured distribution for beam 12, range gate 25 (which is centered in the R2 location), and as before, multiply this value by a randomly selected value from a normal distribution of mean 0 and standard deviation 1. As above, we then combine these measurements to produce a “vorticity” value, and then simulate 10^6 of these values. Figure 7b presents the resulting vorticity PDF (black symbols and lines). The smaller measurement cell size leads to a wider vorticity uncertainty PDF than in R1. The red lines show, for comparison, the PDF for the R2 dusk cell for IMF B_y positive conditions, as shown in Figure 4b. Even though the R2 vorticity uncertainty PDF is wider than that for R1, it still has a lower variance than the observed vorticity PDF in this region, suggesting again that it only has a limited impact on the character of that distribution.

These simulations show that in both R1 and R2, the observed vorticity distributions can be described as being predominantly due to the large and meso-scale flow variations within the SuperDARN measurement cells, and not to measurement and algorithmic errors and uncertainties. In addition, it may in the future be possible to interpret the SuperDARN vorticity uncertainty PDFs in the context of small sub-grid-scale spatiotemporal turbulent structure.

5.2. Interpreting the Model Distributions

The results in this paper have shown that the asymmetric shape of the measured vorticity PDFs in the dayside R1 that have been presented in this and previous papers (Chisham & Freeman, 2010, 2021), can be explained as a mixture of two underlying vorticity distributions: (1) a one-sided distribution that represents the large-scale

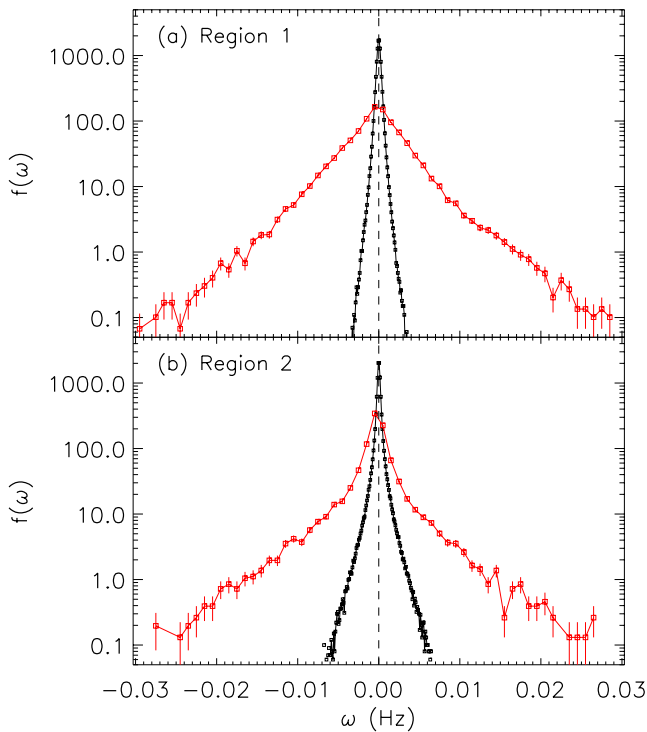


Figure 7. (a) The simulated R1 vorticity uncertainty distribution (black symbols and lines). The red symbols and line present the probability density functions (PDF) for the R1 dusk cell for interplanetary magnetic field (IMF) B_y positive conditions, as shown in Figure 3b, for comparison. (b) The simulated R2 vorticity uncertainty distribution (black symbols and lines). The red symbols and line present the PDF for the R2 dusk cell for IMF B_y positive conditions, as shown in Figure 3b, for comparison.

flow vorticity PDFs varied significantly across the polar ionosphere. In the R1, the vorticity is typically stronger (high κ), but not as intermittent (lower q) as that seen at higher and lower latitudes. This is still the case even after the large-scale component has been removed. It seems possible that this strong vorticity is a result of meso-scale turbulent structure being inherited from the solar wind via magnetic reconnection, as suggested by Abel et al. (2006, 2009, 2007).

The work of Chisham and Freeman (2021) also implies that the nightside R1 meso-scale PDFs are not as wide as those seen on the dayside, which suggests that the nightside does not inherit the same level of turbulent structure from the nightside magnetosphere. It is also possible that differences in conductance between the dayside and nightside ionosphere have a role to play in the observed day-night vorticity PDF differences. A connection to conductance variations may be proved by separating the vorticity PDFs by season, when the levels of conductance across the polar cap will be significantly different due to changes in the extent of photoionization across the polar ionosphere. In order to study the spatial variation of the meso-scale component in more detail requires the systematic separation of the large-scale vorticity component from the PDFs at all locations. Hence, further work is needed to extend the selected-location analysis undertaken in this paper and to separate these components at all measurement locations.

The interpretation of the R2 vorticity variations is much simpler due to the absence of a clear and obvious large-scale convection component in the vorticity PDFs. The vorticity PDFs observed in the R2 are highly symmetric (see Figure 4), and show little variation with IMF direction. They are also very similar on both the dayside and nightside (Chisham & Freeman, 2021). This suggests that the source of the vorticity fluctuations in this region does not vary much with MLT or IMF either. The q -exponential fits to PDFs in this region (Chisham & Freeman, 2021) show that the vorticity is relatively weak (low κ) compared to higher latitudes. However, they also show that the vorticity here is more intermittent (high q). Chisham and Freeman (2021) proposed that the

flow variations that mainly result from the convection driven by magnetic reconnection on the dayside magnetopause; and (2) a symmetric two-sided distribution that represents meso-scale structures in the flow, such as those resulting from turbulence.

The investigations in this paper have focussed mainly on the vorticity PDFs observed in the dayside R1 ionosphere, as this is where these distributions show the most asymmetry (Chisham & Freeman, 2021). Following our assumption that the meso-scale distribution should be symmetric, independent of IMF conditions, any differences between the positive and negative vorticity PDFs (for a fixed IMF) must be due to the addition of a large-scale vorticity component. The large-scale component appears to be well modeled by a Weibull distribution whose presence and polarity vary with IMF B_y in a manner consistent with that expected from dayside magnetopause reconnection.

The work of Chisham and Freeman (2021) showed that smaller asymmetries are typical of the vorticity PDFs observed in the nightside R1 which implies that measurable large-scale vorticity is rarer. This may be consistent with the fact that large-scale vorticities are concentrated into short substorm intervals of strong nightside flows, interspersed with longer quieter intervals with negligible large-scale flow and vorticity (Angelopoulos et al., 1994). This is in contrast to the relatively continuous nature of dayside reconnection. It should be possible to test this hypothesis in the future by comparing the nightside R1 vorticity PDFs measured around the times of substorms with those measured during quieter times.

The meso-scale component PDFs are well modeled by q -exponential distributions. As well as ionospheric vorticity PDFs, q -exponential distributions with high kurtosis have been used to successfully model fluctuations in other space plasma measurements (Barbosa et al., 2017; Burlaga et al., 2007; Coxon et al., 2022; Esquivel & Lazarian, 2010). Chisham and Freeman (2021) showed that the shape and scale of q -exponential fits to the

source of R2 turbulence is fragmented and filamentary FACs in the partial ring current that result in a higher intermittency, and hence, more leptokurtic distributions.

5.3. Impact on the Use of Statistical Models of Ionospheric Plasma Flow

Statistical and climatological models of ionospheric plasma flow (often referred to simply as convection) are increasingly being used in larger M-I system models, or to produce global estimates of secondary data products such as Joule heating (Weimer, 2005). In most instances, these models are determined from statistical averages during particular background environmental conditions (Thomas & Shepherd, 2018; Weimer, 2001). As such, the flow patterns for two very distinct intervals, that occur at times with the same background conditions, will be the same, regardless of other factors. Distributions of fluctuations in the plasma flow, which provide information beyond the average of the observed values, are typically not considered, or assumed to be normally distributed. Not having a full understanding of the distribution of fluctuations of a particular quantity can lead to flawed interpretations of model output and erroneous conclusions (Golovchanskaya, 2008).

The conclusions presented here, that the observed ionospheric vorticity can be described as comprising a mixture of large-scale and meso-scale components has an impact on the way that ionospheric plasma flow is currently modeled. The large-scale component that relates primarily to convection, driven by magnetic reconnection at the Earth's magnetopause and within the Earth's magnetotail, can be viewed as matching the average climatological flow variations seen in statistical maps, and hence this component is well reflected in models. The meso-scale component, that more likely results from processes such as turbulence within the magnetosphere and ionosphere, is unrepresented within statistical maps. The result presented here, that the meso-scale component of ionospheric flow vorticity often has as significant an effect on the flow as the large-scale component, has implications for present models of the ionospheric flow. In order to better match reality, these models would benefit from a stochastic component that represents the turbulent component of the flow. It may be that to fully encompass the effects of this turbulent component, ionospheric flow modeling would benefit from an ensemble forecasting approach, similar to numerical weather prediction.

6. Summary and Conclusions

In this paper we have used a 6-year data set of ionospheric vorticity measured by SuperDARN to investigate the sources of vorticity in the northern hemisphere polar ionosphere. By subdividing the measured PDFs of ionospheric vorticity by the prevailing IMF B_y direction it has allowed the separation of the PDFs into two components.

1. The large-scale vorticity PDFs relate predominantly to the large-scale convection driven by magnetic reconnection. They are single-sided and well fit by Weibull probability distributions.
2. The meso-scale vorticity PDFs relate predominantly to processes such as turbulence. They are double-sided and symmetric, and well fit by q -exponential probability distributions.

Although this work helps to understand the vorticity distributions observed in the R2 and the dayside R1, the nightside R1 needs further investigation, particularly the effect of differences in ionospheric conductance and the impact of substorms. Our observation of a significant meso-scale ionospheric flow vorticity component due to turbulence may have implications for the fidelity of ionospheric plasma flow models that are used in larger-scale system models, which typically only represent the large-scale averaged convection component.

Data Availability Statement

The SuperDARN vorticity data products used in this paper are freely available through Chisham (2023), <https://doi.org/10.5285/8EEDC594-730B-4AAD-B9CE-827912320C3A>. The raw SuperDARN data for this interval are also freely available through the BAS SuperDARN data mirror (<https://www.bas.ac.uk/project/superdarn/>).

Acknowledgments

GC and MPF were supported by the UK Natural Environment Research Council (NERC) highlight topic grant NE/W003066/1 (FINESSE). They were also funded as part of the British Antarctic Survey (BAS) Polar Science for Planet Earth Programme funded by NERC. The authors acknowledge the use of SuperDARN data. SuperDARN is a collection of radars funded by the national scientific funding agencies of Australia, Canada, China, France, Italy, Japan, Norway, South Africa, UK, and United States. The authors would like to thank the SuperDARN PIs of the radars which provided the original data for the vorticity data products: Kathryn McWilliams (University of Saskatchewan, Canada); J. Michael Ruohoniemi (Virginia Tech, USA); William Bristow (Penn State University, USA).

References

- Abel, G. A., Freeman, M. P., & Chisham, G. (2006). Spatial structure of ionospheric convection velocities in regions of open and closed magnetic field topology. *Geophysical Research Letters*, *33*(24), L24103. <https://doi.org/10.1029/2006GL027919>
- Abel, G. A., Freeman, M. P., & Chisham, G. (2009). IMF clock angle control of multifractality in ionospheric velocity fluctuations. *Geophysical Research Letters*, *36*(19), L19102. <https://doi.org/10.1029/2009GL040336>
- Abel, G. A., Freeman, M. P., Chisham, G., & Watkins, N. W. (2007). Investigating turbulent structure of ionospheric plasma velocity using the Halley SuperDARN radar. *Nonlinear Processes in Geophysics*, *14*(6), 799–809. <https://doi.org/10.5194/npg-14-799-2007>
- Anderson, B. J., Korth, H., Waters, C. L., Green, D. L., Merkin, V. G., Barnes, R. J., & Dyrud, L. P. (2014). Development of large-scale Birkeland currents determined from the active magnetosphere and planetary electrodynamics response experiment. *Geophysical Research Letters*, *41*(9), 3017–3025. <https://doi.org/10.1002/2014gl059941>
- Anderson, B. J., Korth, H., Waters, C. L., Green, D. L., & Stauning, P. (2008). Statistical Birkeland current distributions from magnetic field observations by the iridium constellation. *Annales Geophysicae*, *26*(3), 671–687. <https://doi.org/10.5194/angeo-26-671-2008>
- Angelopoulos, V., Kennel, C. F., Coroniti, F. V., Pellat, R., Kivelson, M. G., Walker, R. J., et al. (1994). Statistical characteristics of bursty bulk flow events. *Journal of Geophysical Research*, *99*(A11), 21257–21280. <https://doi.org/10.1029/94ja01263>
- Barbosa, C. S., Caraballo, R., Alves, L. R., Hartmann, G. A., Beggan, C. D., Viljanen, A., et al. (2017). The Tsallis statistical distribution applied to geomagnetically induced currents. *Space Weather*, *15*(9), 1094–1101. <https://doi.org/10.1002/2017SW001631>
- Burlaga, L. F., Vinas, A. F., & Wang, C. (2007). Tsallis distributions of magnetic field strength variations in the heliosphere: 5 to 90 AU. *Journal of Geophysical Research*, *112*, A07206. <https://doi.org/10.1029/2006JA012213>
- Chaston, C. C., Salem, C., Bonnell, J. W., Carlson, C. W., Ergun, R. E., Strangeway, R. J., & McFadden, J. P. (2008). The turbulent Alfvénic aurora. *Physical Review Letters*, *100*(17), 175003. <https://doi.org/10.1103/physrevlett.100.175003>
- Chisham, G. (2017). A new methodology for the development of high-latitude ionospheric climatologies and empirical models. *Journal of Geophysical Research*, *122*(1), 932–947. <https://doi.org/10.1002/2016JA023235>
- Chisham, G. (2023). Ionospheric vorticity across the northern hemisphere ionosphere determined from particular superdarn radar pairs – 2000 to 2005 inclusive (version 1.0). [Dataset]. NERC EDS UK Polar Data Centre, UK Research & Innovation. <https://doi.org/10.5285/8EEDC594-730B-4AAD-B9CE-827912320C3A>
- Chisham, G., & Freeman, M. P. (2010). On the non-Gaussian nature of ionospheric vorticity. *Geophysical Research Letters*, *37*(12), L12103. <https://doi.org/10.1029/2010GL043714>
- Chisham, G., & Freeman, M. P. (2021). A statistical model of vorticity in the polar ionosphere and implications for extreme values. *Journal of Geophysical Research*, *126*(11), e2021JA029307. <https://doi.org/10.1029/2021JA029307>
- Chisham, G., Freeman, M. P., Abel, G. A., Bristow, W. A., Marchaudon, A., Ruohoniemi, J. M., & Sofko, G. J. (2009). Spatial distribution of average vorticity in the high-latitude ionosphere and its variation with interplanetary magnetic field direction and season. *Journal of Geophysical Research*, *114*(A9), A09301. <https://doi.org/10.1029/2009JA014263>
- Chisham, G., Freeman, M. P., Abel, G. A., Lam, M. M., Pinnock, M., Coleman, I. J., et al. (2008). Remote sensing of the spatial and temporal structure of magnetopause and magnetotail reconnection from the ionosphere. *Reviews of Geophysics*, *46*(1), RG1004. <https://doi.org/10.1029/2007RG000223>
- Chisham, G., Lester, M., Milan, S. E., Freeman, M. P., Bristow, W. A., Grocott, A., et al. (2007). A decade of the Super Dual Auroral Radar Network (SuperDARN): Scientific achievements, new techniques and future directions. *Surveys in Geophysics*, *28*(1), 33–109. <https://doi.org/10.1007/s10712-007-9017-8>
- Chisham, G., Yeoman, T. K., & Sofko, G. J. (2008). Mapping ionospheric backscatter measured by the SuperDARN HF radars – Part 1: A new empirical virtual height model. *Annales Geophysicae*, *26*(4), 823–841. <https://doi.org/10.5194/angeo-26-823-2008>
- Cowley, S. W. H., & Lockwood, M. (1992). Excitation and decay of solar wind-driven flows in the magnetosphere-ionosphere system. *Annales Geophysicae*, *10*, 103–115.
- Coxon, J. C., Chisham, G., Freeman, M. P., Anderson, B. J., & Fear, R. C. (2022). Distributions of Birkeland current density observed by AMPERE are heavy-tailed or long-tailed. *Journal of Geophysical Research*, *127*(2), e2021JA029801. <https://doi.org/10.1029/2021JA029801>
- Di Mare, F., Spicher, A., Clausen, L. B. N., Miloch, W. J., & Moen, J. I. (2021). Turbulence and intermittency in the winter cusp ionosphere studied with the ICI sounding rockets. *Journal of Geophysical Research*, *126*(8), e2021JA029150. <https://doi.org/10.1029/2021JA029150>
- Esquivel, A., & Lazarian, A. (2010). Tsallis statistics as a tool for studying interstellar turbulence. *The Astrophysical Journal*, *710*(1), 125–132. <https://doi.org/10.1088/0004-637x/710/1/125>
- Frisch, U. (2010). *Turbulence: The legacy of A. N. Kolmogorov*. Cambridge University Press.
- Golovchanskaya, I. V. (2008). Assessment of Joule heating for the observed distributions of high-latitude electric fields. *Geophysical Research Letters*, *35*(16), L16102. <https://doi.org/10.1029/2008GL034413>
- Greenwald, R. A., Baker, K. B., Dudeney, J. R., Pinnock, M., Jones, T. B., Thomas, E. C., et al. (1995). DARN/Superdarn: A global view of the dynamics of high-latitude convection. *Space Science Reviews*, *71*(1–4), 761–796. <https://doi.org/10.1007/bf00751350>
- Hubert, B., Milan, S. E., Grocott, A., Blockx, C., Cowley, S. W. H., & Gerard, J.-C. (2006). Dayside and nightside reconnection rates inferred from IMAGE-FUV and Super Dual Auroral Radar Network data. *Journal of Geophysical Research*, *111*(A3), A03217. <https://doi.org/10.1029/2005ja011140>
- Iijima, T., & Potemra, T. A. (1976). The amplitude distribution of field-aligned currents at northern high latitudes observed by Triad. *Journal of Geophysical Research*, *81*(13), 2165–2174. <https://doi.org/10.1029/ja081i013p02165>
- Kintner, P. M., & Seyler, C. E. (1985). The status of observations and theory of high latitude ionospheric and magnetospheric plasma turbulence. *Space Science Reviews*, *41*(1–2), 91–129. <https://doi.org/10.1007/bf00241347>
- Lockwood, M., Cowley, S. W. H., & Freeman, M. P. (1990). The excitation of plasma convection in the high-latitude ionosphere. *Journal of Geophysical Research*, *95*(A6), 7961–7972. <https://doi.org/10.1029/ja095ia06p07961>
- Milan, S. E. (2013). Modeling Birkeland currents in the expanding/contracting polar cap paradigm. *Journal of Geophysical Research*, *118*(9), 5532–5542. <https://doi.org/10.1002/jgra.50393>
- Milan, S. E., Gosling, J. S., & Hubert, B. (2012). Relationship between interplanetary parameters and the magnetopause reconnection rate quantified from observations of the expanding polar cap. *Journal of Geophysical Research*, *117*(A3), A03226. <https://doi.org/10.1029/2011JA017082>
- Milan, S. E., Lester, M., Cowley, S. W. H., Oksavik, K., Brittacher, M., Greenwald, R. A., et al. (2003). Variations in the polar cap area during two substorm cycles. *Annales Geophysicae*, *21*(5), 1121–1140. <https://doi.org/10.5194/angeo-21-1121-2003>
- Nishitani, N., Ruohoniemi, J. M., Lester, M., Baker, J. B. H., Koustov, A. V., Shepherd, S. G., et al. (2019). Review of the accomplishments of mid-latitude Super Dual Auroral Radar Network (SuperDARN) HF radars. *Progress in Earth and Planetary Science*, *6*(1), 27. <https://doi.org/10.1186/s40645-019-0270-5>

- Siscoe, G. L., & Huang, T. S. (1985). Polar cap inflation and deflation. *Journal of Geophysical Research*, *90*(A1), 543–547. <https://doi.org/10.1029/ja090ia01p00543>
- Sofko, G. J., Greenwald, R. A., & Bristow, W. (1995). Direct determination of large-scale magnetospheric field-aligned currents with SuperDARN. *Geophysical Research Letters*, *22*(15), 2041–2044. <https://doi.org/10.1029/95gl01317>
- Spicher, A., LaBelle, J., Bonnell, J. W., Roglans, R., Moser, C., Fuselier, S. A., et al. (2022). Interferometric study of ionospheric plasma irregularities in regions of phase scintillations and HF backscatter. *Geophysical Research Letters*, *49*(12), e2021GL097013. <https://doi.org/10.1029/2021GL097013>
- Spicher, A., Miloch, W. J., Clausen, L. B. N., & Moen, J. I. (2015). Plasma turbulence and coherent structures in the polar cap observed by the ICI-2 sounding rocket. *Journal of Geophysical Research*, *120*(12), 10959–10978. <https://doi.org/10.1002/2015ja021634>
- Thomas, E. G., & Shepherd, S. G. (2018). Statistical patterns of ionospheric convection derived from mid-latitude, high-latitude, and polar SuperDARN HF radar observations. *Journal of Geophysical Research*, *123*(4), 3196–3216. <https://doi.org/10.1002/2018ja025280>
- Tsunoda, R. T. (1988). High latitude F-region irregularities: A review and synthesis. *Reviews of Geophysics*, *26*(4), 719–760. <https://doi.org/10.1029/rg026i004p00719>
- Vallières, X., Villain, J.-P., Hanuise, C., & André, R. (2004). Ionospheric propagation effects on spectral widths measured by SuperDARN HF radars. *Annales Geophysicae*, *22*(6), 2023–2031. <https://doi.org/10.5194/angeo-22-2023-2004>
- Waters, C. L., Anderson, B. J., & Liou, K. (2001). Estimation of global field-aligned currents using the Iridium System magnetometer data. *Geophysical Research Letters*, *28*(11), 2165–2168. <https://doi.org/10.1029/2000gl012725>
- Weimer, D. R. (2001). An improved model of ionospheric electric potentials including substorm perturbations and application to the geospace environment modeling November 24 1996 event. *Journal of Geophysical Research*, *106*(A1), 407–416. <https://doi.org/10.1029/2000ja000604>
- Weimer, D. R. (2005). Improved ionospheric electrodynamic models and application to calculating Joule heating rates. *Journal of Geophysical Research*, *110*(A5), A05306. <https://doi.org/10.1029/2004JA010884>

Erratum

The originally published version of this article contained typographical errors. The fifth sentence of the sixth paragraph of Section 3 should read: “These PDFs are determined from 51,042 and 30,240 ...”. The fifth sentence of the seventh paragraph of Section 3 should read: “These PDFs are determined from 29,678 and 36,860 ...”. The fifth sentence of the ninth paragraph of Section 3 should read: “The PDFs for the dawn cell are determined from 29,002 and 32,056 ...”. The sixth sentence of the ninth paragraph of Section 3 should read: “The PDFs for the dusk cell are determined from 15,278 and 21,046 ...”. The errors have been corrected, and this may be considered the authoritative version of record.